Biomedical Optics EXPRESS

# Parametric imaging of the local attenuation coefficient in human axillary lymph nodes assessed using optical coherence tomography

**Loretta Scolaro,[1,*] Robert A. McLaughlin,[1] Blake R. Klyen,[1] Benjamin A. Wood,[2] Peter D. Robbins,[2] Christobel M. Saunders,[3,4] Steven L. Jacques,[5] and David D. Sampson[1,6]**

[1]*Optical + Biomedical Engineering Laboratory, School of Electrical, Electronic, and Computer Engineering, The University of Western Australia, Crawley, Australia*
[2]*PathWest Laboratory Medicine WA, QEII Medical Centre, Nedlands, Western Australia, Australia*
[3]*School of Surgery, The University of Western Australia, Crawley, Australia*
[4]*Sir Charles Gairdner Hospital, Nedlands, Western Australia, Australia*
[5]*Departments of Dermatology and Biomedical Engineering, Oregon Health and Science University, Portland, Oregon, USA*
[6]*Centre for Microscopy, Characterisation and Analysis, The University of Western Australia, Crawley, Australia*
**lscolaro@ee.uwa.edu.au*

**Abstract:** We report the use of optical coherence tomography (OCT) to determine spatially localized optical attenuation coefficients of human axillary lymph nodes and their use to generate parametric images of lymphoid tissue. 3D-OCT images were obtained from excised lymph nodes and optical attenuation coefficients were extracted assuming a single scattering model of OCT. We present the measured attenuation coefficients for several tissue regions in benign and reactive lymph nodes, as identified by histopathology. We show parametric images of the measured attenuation coefficients as well as segmented images of tissue type based on thresholding of the attenuation coefficient values. Comparison to histology demonstrates the enhancement of contrast in parametric images relative to OCT images. This enhancement is a step towards the use of OCT for *in situ* assessment of lymph nodes.



**OCIS codes:** (110.4500) Optical coherence tomography; (170.6935) Tissue characterization.

## References

1. M. Cianfrocca and L. J. Goldstein, "Prognostic and predictive factors in early-stage breast cancer," Oncologist **9**(6), 606–616 (2004).
2. U. Veronesi, G. Viale, G. Paganelli, S. Zurrida, A. Luini, V. Galimberti, P. Veronesi, M. Intra, P. Maisonneuve, F. Zucca, G. Gatti, G. Mazzarol, C. De Cicco, and D. Vezzoli, "Sentinel lymph node biopsy in breast cancer: ten-year results of a randomized controlled study," Ann. Surg. **251**(4), 595–600 (2010).
3. J. A. Petrek, R. T. Senie, M. Peters, and P. P. Rosen, "Lymphedema in a cohort of breast carcinoma survivors 20 years after diagnosis," Cancer **92**(6), 1368–1377 (2001).
4. U. Veronesi, G. Paganelli, V. Galimberti, G. Viale, S. Zurrida, M. Bedoni, A. Costa, C. de Cicco, J. G. Geraghty, A. Luini, V. Sacchini, and P. Veronesi, "Sentinel-node biopsy to avoid axillary dissection in breast cancer with clinically negative lymph-nodes," Lancet **349**(9069), 1864–1867 (1997).
5. L. G. Wilke, L. M. McCall, K. E. Posther, P. W. Whitworth, D. S. Reintgen, A. M. Leitch, S. G. A. Gabram, A. Lucci, C. E. Cox, K. K. Hunt, J. E. Herndon 2nd, and A. E. Giuliano, "Surgical complications associated with sentinel lymph node biopsy: results from a prospective international cooperative group trial," Ann. Surg. Oncol. **13**(4), 491–500 (2006).
6. T. Kim, A. E. Giuliano, and G. H. Lyman, "Lymphatic mapping and sentinel lymph node biopsy in early-stage breast carcinoma," Cancer **106**(1), 4–16 (2006).
7. K. J. Rosbach, D. Shin, T. J. Muldoon, M. A. Quraishi, L. P. Middleton, K. K. Hunt, F. Meric-Bernstam, T. K. Yu, R. R. Richards-Kortum, and W. Yang, "High-resolution fiber optic microscopy with fluorescent contrast enhancement for the identification of axillary lymph node metastases in breast cancer: a pilot study," Biomed. Opt. Express **1**(3), 911–922 (2010).
8. K. S. Johnson, D. W. Chicken, D. C. O. Pickard, A. C. Lee, G. Briggs, M. Falzon, I. J. Bigio, M. R. Keshtgar, and S. G. Bown, "Elastic scattering spectroscopy for intraoperative determination of sentinel lymph node status in the breast," J. Biomed. Opt. **9**(6), 1122–1128 (2004).

#158284 - $15.00 USD Received 18 Nov 2011; revised 9 Jan 2012; accepted 18 Jan 2012; published 27 Jan 2012

9. M. R. S. Keshtgar, D. W. Chicken, M. R. Austwick, S. K. Somasundaram, C. A. Mosse, Y. Zhu, I. J. Bigio, and S. G. Bown, "Optical scanning for rapid intraoperative diagnosis of sentinel node metastases in breast cancer," Br. J. Surg. **97**(8), 1232–1239 (2010).
10. W. Luo, F. T. Nguyen, A. M. Zysk, T. S. Ralston, J. Brockenbrough, D. L. Marks, A. L. Oldenburg, and S. A. Boppart, "Optical biopsy of lymph node morphology using optical coherence tomography," Technol. Cancer Res. Treat. **4**(5), 539–548 (2005).
11. R. A. McLaughlin, L. Scolaro, P. Robbins, S. Hamza, C. Saunders, and D. D. Sampson, "Imaging of human lymph nodes using optical coherence tomography: potential for staging cancer," Cancer Res. **70**(7), 2579–2584 (2010).
12. F. T. Nguyen, A. M. Zysk, E. J. Chaney, S. G. Adie, J. G. Kotynek, U. J. Oliphant, F. J. Bellafiore, K. M. Rowland, P. A. Johnson, and S. A. Boppart, "Optical coherence tomography: the intraoperative assessment of lymph nodes in breast cancer," IEEE Eng. Med. Biol. Mag. **29**(2), 63–70 (2010).
13. Y. Jung, Z. Zhi, and R. K. Wang, "Three-dimensional optical imaging of microvascular networks within intact lymph node in vivo," J. Biomed. Opt. **15**(5), 050501 (2010).
14. J. M. Schmitt, A. Knüttel, and R. F. Bonner, "Measurement of optical properties of biological tissues by low-coherence reflectometry," Appl. Opt. **32**(30), 6032–6042 (1993).
15. D. J. Faber, F. J. van der Meer, M. C. G. Aalders, and T. G. van Leeuwen, "Quantitative measurement of attenuation coefficients of weakly scattering media using optical coherence tomography," Opt. Express **12**(19), 4353–4365 (2004).
16. D. Levitz, M. T. Hinds, N. Choudhury, N. T. Tran, S. R. Hanson, and S. L. Jacques, "Quantitative characterization of developing collagen gels using optical coherence tomography," J. Biomed. Opt. **15**(2), 026019 (2010).
17. I. V. Turchin, E. A. Sergeeva, L. S. Dolin, V. A. Kamensky, N. M. Shakhova, and R. Richards-Kortum, "Novel algorithm of processing optical coherence tomography images for differentiation of biological tissue pathologies," J. Biomed. Opt. **10**(6), 064024 (2005).
18. F. J. van der Meer, D. J. Faber, D. M. B. Sassoon, M. C. Aalders, G. Pasterkamp, and T. G. van Leeuwen, "Localized measurement of optical attenuation coefficients of atherosclerotic plaque constituents by quantitative optical coherence tomography," IEEE Trans. Med. Imaging **24**(10), 1369–1376 (2005).
19. A. Knüttel, S. Bonev, and W. Knaak, "New method for evaluation of in vivo scattering and refractive index properties obtained with optical coherence tomography," J. Biomed. Opt. **9**(2), 265–273 (2004).
20. T. Q. Xie, M. L. Zeidel, and Y. T. Pan, "Detection of tumorigenesis in urinary bladder with optical coherence tomography: optical characterization of morphological changes," Opt. Express **10**(24), 1431–1443 (2002).
21. S. W. Jeon, M. A. Shure, K. B. Baker, D. Huang, A. M. Rollins, A. Chahlavi, and A. R. Rezai, "A feasibility study of optical coherence tomography for guiding deep brain probes," J. Neurosci. Methods **154**(1-2), 96–101 (2006).
22. K. Barwari, D. M. de Bruin, E. C. C. Cauberg, D. J. Faber, T. G. van Leeuwen, H. Wijkstra, J. de la Rosette, and M. P. Laguna, "Advanced diagnostics in renal mass using optical coherence tomography: a preliminary report," J. Endourol. **25**(2), 311–315 (2011).
23. R. A. McLaughlin, L. Scolaro, P. Robbins, C. Saunders, S. L. Jacques, and D. D. Sampson, "Parametric imaging of cancer with optical coherence tomography," J. Biomed. Opt. **15**(4), 046029 (2010).
24. J. M. Schmitt, A. Knüttel, M. Yadlowsky, and M. A. Eckhaus, "Optical-coherence tomography of a dense tissue: statistics of attenuation and backscattering," Phys. Med. Biol. **39**(10), 1705–1720 (1994).
25. C. Y. Xu, J. M. Schmitt, S. G. Carlier, and R. Virmani, "Characterization of atherosclerosis plaques by measuring both backscattering and attenuation coefficients in optical coherence tomography," J. Biomed. Opt. **13**(3), 034003 (2008).
26. A. Miyazawa, M. Yamanari, S. Makita, M. Miura, K. Kawana, K. Iwaya, H. Goto, and Y. Yasuno, "Tissue discrimination in anterior eye using three optical parameters obtained by polarization sensitive optical coherence tomography," Opt. Express **17**(20), 17426–17440 (2009).
27. E. C. C. Cauberg, D. M. de Bruin, D. J. Faber, T. M. de Reijke, M. Visser, J. J. M. C. H. de la Rosette, and T. G. van Leeuwen, "Quantitative measurement of attenuation coefficients of bladder biopsies using optical coherence tomography for grading urothelial carcinoma of the bladder," J. Biomed. Opt. **15**(6), 066013 (2010).
28. A. Knüttel and M. Boehlau-Godau, "Spatially confined and temporally resolved refractive index and scattering evaluation in human skin performed with optical coherence tomography," J. Biomed. Opt. **5**(1), 83–92 (2000).
29. A. I. Kholodnykh, I. Y. Petrova, M. Motamedi, and R. O. Esenaliev, "Accurate measurement of total attenuation coefficient of thin tissue with optical coherence tomography," IEEE J. Sel. Top. Quantum Electron. **9**(2), 210–221 (2003).
30. G. van Soest, T. Goderie, E. Regar, S. Koljenović, G. L. J. H. van Leenders, N. Gonzalo, S. van Noorden, T. Okamura, B. E. Bouma, G. J. Tearney, J. W. Oosterhuis, P. W. Serruys, and A. F. W. van der Steen, "Atherosclerotic tissue characterization in vivo by optical coherence tomography attenuation imaging," J. Biomed. Opt. **15**(1), 011105 (2010).
31. L. Thrane, H. T. Yura, and P. E. Andersen, "Analysis of optical coherence tomography systems based on the extended Huygens-Fresnel principle," J. Opt. Soc. Am. A **17**(3), 484–490 (2000).
32. J. N. Qu, C. Macaulay, S. Lam, and B. Palcic, "Optical properties of normal and carcinomatous bronchial tissue," Appl. Opt. **33**(31), 7397–7405 (1994).
33. T. G. van Leeuwen, D. J. Faber, and M. C. Aalders, "Measurement of the axial point spread function in scattering media using single-mode fiber-based optical coherence tomography," IEEE J. Sel. Top. Quantum Electron. **9**(2), 227–233 (2003).

#158284 - $15.00 USD Received 18 Nov 2011; revised 9 Jan 2012; accepted 18 Jan 2012; published 27 Jan 2012

34. B. R. Klyen, T. Shavlakadze, H. G. Radley-Crabb, M. D. Grounds, and D. D. Sampson, "Identification of muscle necrosis in the *mdx* mouse model of Duchenne muscular dystrophy using three-dimensional optical coherence tomography," J. Biomed. Opt. **16**(7), 076013 (2011).
35. X. Y. Ma, J. Q. Lu, R. S. Brock, K. M. Jacobs, P. Yang, and X. H. Hu, "Determination of complex refractive index of polystyrene microspheres from 370 to 1610 nm," Phys. Med. Biol. **48**(24), 4165–4172 (2003).
36. C. Flueraru, D. P. Popescu, Y. Mao, S. Chang, and M. G. Sowa, "Added soft tissue contrast using signal attenuation and the fractal dimension for optical coherence tomography images of porcine arterial tissue," Phys. Med. Biol. **55**(8), 2317–2331 (2010).
37. T. Durduran, R. Choe, J. P. Culver, L. Zubkov, M. J. Holboke, J. Giammarco, B. Chance, and A. G. Yodh, "Bulk optical properties of healthy female breast tissue," Phys. Med. Biol. **47**(16), 2847–2861 (2002).
38. F. J. van der Meer, D. J. Faber, M. C. G. Aalders, A. A. Poot, I. Vermes, and T. G. van Leeuwen, "Apoptosis- and necrosis-induced changes in light attenuation measured by optical coherence tomography," Lasers Med. Sci. **25**(2), 259–267 (2010).
39. B. D. Goldberg, N. V. Iftimia, J. E. Bressner, M. B. Pitman, E. Halpern, B. E. Bouma, and G. J. Tearney, "Automated algorithm for differentiation of human breast tissue using low coherence interferometry for fine needle aspiration biopsy guidance," J. Biomed. Opt. **13**(1), 014014 (2008).
40. N. V. Iftimia, B. E. Bouma, M. B. Pitman, B. Goldberg, J. Bressner, and G. J. Tearney, "A portable, low coherence interferometry based instrument for fine needle aspiration biopsy guidance," Rev. Sci. Instrum. **76**(6), 064301 (2005).
41. A. M. Zysk and S. A. Boppart, "Computational methods for analysis of human breast tumor tissue in optical coherence tomography images," J. Biomed. Opt. **11**(5), 054015 (2006).
42. M. Mujat, R. D. Ferguson, D. X. Hammer, C. Gittins, and N. Iftimia, "Automated algorithm for breast tissue differentiation in optical coherence tomography," J. Biomed. Opt. **14**(3), 034040 (2009).
43. R. A. McLaughlin, B. C. Quirk, A. Curatolo, R. W. Kirk, L. Scolaro, D. Lorenser, P. D. Robbins, B. A. Wood, C. M. Saunders, and D. D. Sampson, "Imaging of breast cancer with optical coherence tomography needle probes: feasibility and initial results," IEEE J. Sel. Topics Quantum Electron. (to be published).
44. B. Pritt, J. J. Tessitore, D. L. Weaver, and H. Blaszyk, "The effect of tissue fixation and processing on breast cancer size," Hum. Pathol. **36**(7), 756–760 (2005).
45. P. L. Hsiung, P. R. Nambiar, and J. G. Fujimoto, "Effect of tissue preservation on imaging using ultrahigh resolution optical coherence tomography," J. Biomed. Opt. **10**(6), 064033 (2005).

## 1. Introduction

The lymphatic system, which comprises the network of nodes and vessels through which lymph circulates throughout the body, is a common pathway for the metastatic spread of cancer. For patients with early stage breast cancer, the presence or absence of malignant deposits in axillary lymph nodes is the single most important prognostic indicator [1].

Histological assessment of excised lymph nodes is the current gold standard for determining lymph node status (i.e. the presence or absence of metastatic deposits) in patients with malignancy. Dissection of most or all of the axillary lymph nodes (axillary clearance) is a standard surgical treatment for breast cancer patients with metastatic involvement of lymph nodes, having both a therapeutic and diagnostic function [2]. However, the procedure may be complicated by lymphedema, the chronic swelling and immovability of the arm caused by fluid retention from disruption of lymphatic pathways [3].

Sentinel lymph node biopsy is a common procedure to assess axillary lymph node status and avoid the significant morbidity associated with axillary clearance if the biopsied node is healthy [4]. The procedure involves removal of only the first lymph node on the lymphatic pathways draining a tumor. Even though sentinel node biopsy is less invasive than axillary clearance, lymphedema still occurs in up to 7% of patients [5]. Furthermore, only 42% of sentinel nodes contain metastases [6], indicating that uninvolved 'healthy' lymph nodes are excised in a significant proportion of cases.

Alternative optical assessment techniques have been investigated with the goal of reducing the number of excised nodes. These techniques include fluorescence molecular imaging [7], elastic scattering spectroscopy [8,9] and optical coherence tomography (OCT) [10–13]. In previous studies, metastatic deposits in lymph nodes imaged with OCT were observed as regions of higher scattering relative to surrounding normal tissue, confirmed by comparison to histological sections [10,11]. In another study, metastatic lymph nodes were identified based on the loss of definition of the capsule/lymphoid junction when imaged with OCT through the capsule [12]. Such cancer detection with OCT is qualitative, as it is based on contrast that, for the same nominal tissue structure, can vary due to imaging artifacts and system variations. As a result, OCT images may not be comparable between different systems or different scanning

#158284 - $15.00 USD Received 18 Nov 2011; revised 9 Jan 2012; accepted 18 Jan 2012; published 27 Jan 2012

sessions. This lack of repeatability presents a significant barrier to the clinical adoption of OCT.

Quantitative measurement of optical properties based on analysis of OCT image data is a potential means of providing such repeatable contrast. Optical properties describe light propagation in tissue and have been measured assuming several models of OCT signal formation [14–16]. Optical properties such as the attenuation coefficient and backscattering coefficient have been extracted for healthy and diseased tissues of the cervix [17], arterial segments [18], human skin [19] and other tissues [14,20–22]. Earlier work has reported parametric OCT imaging of lymph nodes based on the relative optical attenuation coefficient extracted from OCT A-scans [23]. This work showed a qualitative improvement in the differentiation of diffuse cancer and residual normal cortical tissue; however, absolute attenuation coefficients were not obtained and this work did not provide a characterization of healthy lymphoid tissues.

In this paper, we take the next step in establishing the optical properties corresponding to lymph node pathology. We present a methodology to evaluate the absolute attenuation coefficients in excised human axillary lymph nodes. We extract local attenuation coefficients from 3D-OCT volumes and use these to generate quantitative parametric OCT images. We report ranges of attenuation coefficients of selected tissue regions and present parametric maps of tissue type based on these ranges. We verify the resulting mapping through correlation with histology and demonstrate that quantitative parametric OCT images provide improved differentiation of tissue type compared to standard OCT backscatter images alone.

## 2. OCT signal model

In the single-scattering model of light propagation in tissue, light contributing to the OCT signal is assumed to have experienced only a single back-scattering event. This model has been extensively applied for measuring optical attenuation of tissues *ex vivo* [18,24–27] and *in vivo* [28–30]. A model accounting for multiple scattering was also developed for highly turbid samples [31]. We employ the single-scattering model due to its simplicity and robustness in describing the OCT signal at low optical depths. Briefly, the returning power fraction, or reflectance $R(z)$, of light detected from a homogeneous tissue is determined from the exponential decay of irradiance versus depth $z$, in accordance with the Beer-Lambert law,

$$R(z) = \rho e^{-2\mu_t z}. \tag{1}$$

The attenuation coefficient $\mu_t$ ($\text{mm}^{-1}$) describes this decay and is a result of scattering and absorption. The contribution of tissue absorption is very low at the near infrared wavelengths used in OCT and can be considered negligible in comparison to scattering [32]. The factor of 2 in the exponent accounts for the double pass that singly back-scattered light makes through the tissue and $\rho$ is the local reflectance given by the initial value of the reflectance, $R(z=0)$.

The square of the detected OCT photocurrent $i^2(z)$, is a linear function of the reflectance $R(z)$, and is modulated by system factors such as the numerical aperture of the optics and the OCT depth scan response. The OCT signal can be modeled as

$$i^2(z) \propto F(z)S(z)R(z), \tag{2}$$

where $F(z)$ represents the modulation due to the confocal aperture of the OCT system, and $S(z)$ represents the modulation due to the OCT depth scan response. $F(z)$ depends on the focusing and collection optics and has previously been termed a beam-divergence function [14], a confocal function [29], or an axial point spread function [33]. $S(z)$ arises from coupling loss due to scanning the reference arm in time-domain OCT or from sensitivity drop-off in spectral-domain OCT. To correct for these modulations for our time-domain OCT system, we measured the signal from a homogeneous diffuse scattering phantom with known reference optical properties, $\mu_{to}$ and $\rho_o$ (where the subscript $o$ denotes a property of the phantom).

#158284 - $15.00 USD Received 18 Nov 2011; revised 9 Jan 2012; accepted 18 Jan 2012; published 27 Jan 2012

Since the modulation functions are an implicit component of the OCT signal from the homogeneous phantom $i_o^2(z)$, then

$$i_o^2(z) \propto F(z)S(z)R_o(z), \tag{3}$$

with

$$R_o(z) = \rho_o e^{-2\mu_{to}z}. \tag{4}$$

Dividing the OCT signal acquired from a tissue by that from the homogeneous phantom, the tissue attenuation referenced to that of the phantom can be obtained:

$$\frac{i_s^2(x,y,z)}{i_o^2(x,y,z)} \propto \left(\frac{\rho}{\rho_o}\right) e^{\left(-2(\mu_t-\mu_{to})z\right)}. \tag{5}$$

To determine the theoretical values of $\mu_{to}$ for the phantom, we used Mie theory to calculate the scattering coefficient $\mu_{so}$ and anisotropy $g_o$, and relate these to the total attenuation [16]

$$\mu_{to} = \mu_{so} G a(g_o), \tag{6}$$

where $G$ is a factor accounting for the extra path length of light rays travelling obliquely towards the focus (approximately one for the low numerical aperture used in OCT). The function $a(g)$ gives a fraction between zero and one that diminishes the attenuation by taking into account forward scattered photons that, by nature of their forward trajectory, do not contribute to signal loss with depth. The function for $a(g)$ was determined using Monte Carlo modeling and is given by [16]

$$a(g) = 1 - e^{\frac{-(1-g)^{0.6651}}{0.1555}}. \tag{7}$$

The correction phantoms for this study are described in Section 3.3 below. Lymph node tissue was assumed to consist of homogeneous regions of single tissue types sufficiently large to employ Eq. (5) and extract $\mu_t$ from the measured signal decay in each region. By subsequent careful assessment of tissue regions, the attenuation coefficient ranges for different lymphoid tissue types were determined.

## 3. Materials and methods

### *3.1 Optical coherence tomography imaging*

The OCT system used for generating three-dimensional data for imaging and attenuation measurement has been previously described [34]. The custom-built time-domain OCT scanner has a source center wavelength of 1320 nm and a 3-dB bandwidth of 154 nm (DenseLight Semiconductors, Singapore). The sample arm consists of an objective lens with a measured numerical aperture of 0.07, and a transverse scanning assembly with a scanning range (*x*-*y*) of 3.5 × 6 mm. The measured lateral resolution of this assembly, given by the $1/e^2$ beam diameter at the beam waist is ~11 μm in air. The measured axial resolution, given by the full width at half maximum of the axial point spread function is ~8 μm in air. Axial scanning was performed using a frequency-domain optical delay line in the reference arm that gave an axial scan range of 2.2 mm in air and an axial scan rate of 500Hz. The acquisition time for a full 3D-OCT image was 30 minutes. The sampling density for these studies was 2.1 μm per pixel in the axial direction, and 3.4 and 5.9 μm per pixel in the *x* and *y* lateral directions, respectively. The interference signal was detected using dual-balanced photodetectors, and the measured photocurrent converted to a voltage signal. The voltage signal was processed in hardware by band-pass filtering for noise reduction and signal smoothing, and logarithmic demodulation for envelope detection. The signal was acquired for processing after analog-to-digital conversion with a detection sensitivity of −104 dB.

#158284 - $15.00 USD Received 18 Nov 2011; revised 9 Jan 2012; accepted 18 Jan 2012; published 27 Jan 2012

Samples were imaged from below through a glass window, which was oriented perpendicular to the imaging beam. A layer of phosphate-buffered saline (PBS) (n = 1.32) was employed between the glass window and lymph node samples, which improved refractive index matching and reduced the intensity of the specular reflection. Lymph node samples were imaged either through the capsule or from an exposed cut surface of the node. The focal plane of the imaging beam was set 500 μm (in air) beyond the window/tissue interface. Using geometrical optics to determine the change in refraction at the glass/tissue interface, the focal point changed to a depth of approximately 700 μm in tissue assuming a bulk group refractive index $n_{tissue}$ ~1.4.

### *3.2 Sample preparation and histopathology*

Four axillary lymph nodes were obtained from breast cancer patients at Sir Charles Gairdner Hospital, Western Australia (SCGH). One was from a sentinel node biopsy, two were from axillary clearances from patients with early breast cancer, and the fourth was from an axillary clearance in a patient with advanced breast cancer who had received pre-operative adjuvant therapy. The protocol for this study was reviewed and approved by the SCGH Human Research Ethics Committee. Informed consent to use tissue was obtained from patients prior to surgery. After excision, lymph nodes were cut into 2mm-thick sections for assessment in accordance with standard procedure (PathWest Laboratory Medicine, Western Australia). A total of nine 2mm-thick samples were obtained and underwent OCT imaging within seven hours of excision. Samples were kept hydrated in PBS prior to imaging.

Immediately following OCT imaging, samples were fixed in 4% w/v paraformaldehyde and prepared for histological processing. Fixed samples were paraffin embedded and a 5 μm thick section was cut at approximately 200 μm from the tissue surface. The section was stained with hematoxylin and eosin (H&E) for light microscopy analysis and digital image capture (Scanscope XT, Aperio Technologies Inc., Vista, California) and subsequent co-registration with OCT.

An experienced pathologist identified morphologically distinct regions and tissue structures (referred to here as tissue types) from the digital H&E-stained histology images. Identification of these tissue types facilitated comparison of the histology with the OCT images and the subsequently generated parametric attenuation images. The OCT data was displayed using in-house visualization software developed in C++, which allowed extraction of an arbitrary oblique imaging plane from the 3D-OCT data set. This technique, referred to as multiplanar reformatting in other medical imaging modalities, uses elementary linear algebra to generate the intersection of the 3D data volume with an arbitrary imaging plane. This allows visualization of imaging planes oriented at an angle to the *en face* directions to account for rotation of the histological specimens during fixation and processing. Histology and OCT images were manually co-registered by finding the optimal oblique plane in the 3D-OCT data set to visually match each histological section. Co-registered images were used to identify locations in the OCT volume at which to measure localized attenuation coefficients.

### *3.3 Calibration and correction of A-scans*

#### Calibration

Envelope detected OCT voltages were calibrated to corresponding values of reflectance at the sample using the known reflectance from a glass/air interface (4.05% reflectance at the imaging beam focus). The imaging beam was attenuated using neutral density filters to generate a range of lower reflectance values and corresponding voltages, extending over the dynamic range of the system. Curve fitting of sample reflectance to log-demodulated OCT voltage was used to generate an empirical calibration curve with which to calibrate A-scans.

#### Correction

Uniform diffuse-scattering phantoms were imaged to measure and correct for the confocal and OCT depth scan response modulations in calibrated sample A-scans. The correction phantoms

#158284 - $15.00 USD Received 18 Nov 2011; revised 9 Jan 2012; accepted 18 Jan 2012; published 27 Jan 2012

comprised of homogeneous suspensions of polystyrene microspheres (Polybead®, Polysciences, Inc., USA) diluted in distilled water. Their optical properties were calculated using Mie theory with $n_{water}$ = 1.322 and $n_{polystyrene}$ = 1.574 at 1320 nm [35]. The correction phantoms were imaged immediately prior to lymph node imaging. OCT images of a representative correction phantom (mean microsphere diameter = 0.457 μm, standard deviation = 0.011, concentration = 0.236% solids w/v) are presented in Fig. 1 and highlight the confocal and scanning modulations over the two orthogonal planes of imaging. From Mie theory and Eq. (6), with $G$ = 1 and $a(g_o) = 0.98$, we calculated $\mu_{to} = 0.69$ mm$^{-1}$ for this phantom.

Correction profiles were generated by averaging 77 A-scans at every lateral ($x$,$y$) position of the calibrated phantom data set in order to reduce the contribution of speckle noise to the correction (see Fig. 1(C)). The value of 77 was empirically chosen to be consistent with the 35 × 35 μm (11 × 7 pixel) spatial averaging used to generate the final fitting profiles for tissue, as described in Section 3.4 below. These profiles were used to correct each lymph node data set as per Eq. (5) by dividing lymph node A-scans by the corresponding correction profile over depths at which the A-scan signal was above the noise floor.

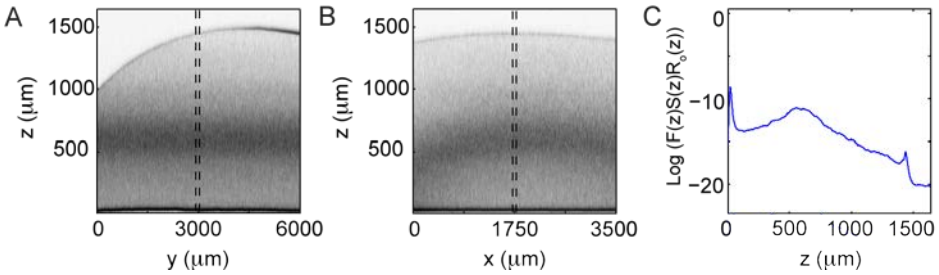


Fig. 1. OCT cross-sectional images of a representative microsphere correction phantom highlighting the confocal and scanning modulations over the (**A**) ($y$-$z$) range; and (**B**) ($x$-$z$) range. (**C**) Correction profile generated from the correction phantom 3D-OCT data set over the region indicted by the dotted lines in A and B. The back interface of the phantom is visible as the curved surface in the cross-sectional images and as a sharp peak of lower-intensity in the correction profile.

### *3.4 Data analysis*

All data analysis was performed in MATLAB® 2009b (The Mathworks, Inc.) using Linux on a 16GB, Intel Quad Core i7, 2.80GHz machine. Custom algorithms were used to process, calibrate and correct 3D-OCT data sets and extract attenuation coefficients. Lymph node A-scans were calibrated before being corrected with appropriate correction profiles to obtain final sample reflectance profiles. Prior to extraction of the attenuation coefficient, speckle noise was reduced by averaging reflectance profiles over a moving window 35 μm wide in both $x$ and $y$ directions (11 × 7 pixels, respectively).

Attenuation coefficients were extracted using linear least-squares regression to fit the log of the averaged reflectance profiles. Fitting was performed over an axial range of 200 μm. Measurements were made at selected points by centering this range at the desired $x$, $y$, $z$ location. The $z$-axis was scaled to correct for the difference between optical and physical path length in tissue, assuming a bulk group refractive index, $n_{tissue}$ = 1.4. Therefore, measured attenuation coefficients correspond to physical depth. The location of the window/tissue interface was set to $z$ = 0 and *en face* parametric images were generated at selected depths $z$, by plotting the measured attenuation coefficients for each ($x$,$y$) location in the *en face* plane. A single parametric image required approximately 20 minutes to be generated on the machine described. Note that the algorithm implementation was not optimized for speed, but does lend itself to significant parallelization in future implementations. Parametric volumes were also generated by automating this process for several depths up to a maximum depth given by $\mu_t z \le 3$ (~250 μm) in order to restrict fitting to regions where single scattering dominates.

#158284 - $15.00 USD Received 18 Nov 2011; revised 9 Jan 2012; accepted 18 Jan 2012; published 27 Jan 2012

The visualization of parametric images at several depths facilitated the mapping of attenuation values to the corresponding histology.

Two homogeneous microsphere tissue phantoms were imaged to investigate the goodness-of-fit of the least-squares regression. Linear least-squares regression for both phantoms gave median $R^2$ values of 0.7. Therefore, fits with $R^2 < 0.70$ were rejected for parametric images. A more stringent requirement of $R^2 > 0.98$ was used for recording attenuation coefficient ranges with improved accuracy, as these values were used to color map subsequent data.

## 4. Results

### *4.1 Attenuation coefficients of lymphoid tissue*

The attenuation coefficients were measured from selected locations within each of the nine lymph node sections imaged. A representative result from a healthy lymph node is presented in Fig. 2. Tissue regions of interest, identified from the corresponding H&E-stained histology in Fig. 2(A) are medulla, paracortex, fibrous capsule and adipose. The medulla is characterized by medullary sinuses (MS) traversed by light-pink staining fine reticular fibers and large pale-staining histiocytes. The sinuses are interspersed between cords of small, round, dark-purple staining lymphocytes. Lymphocytes also make up the surrounding paracortex (P), which also contains small blood venules and larger cells within a fibrous stroma. The thin, pink-staining fibrous capsule (FC) encases the lymph node and is composed

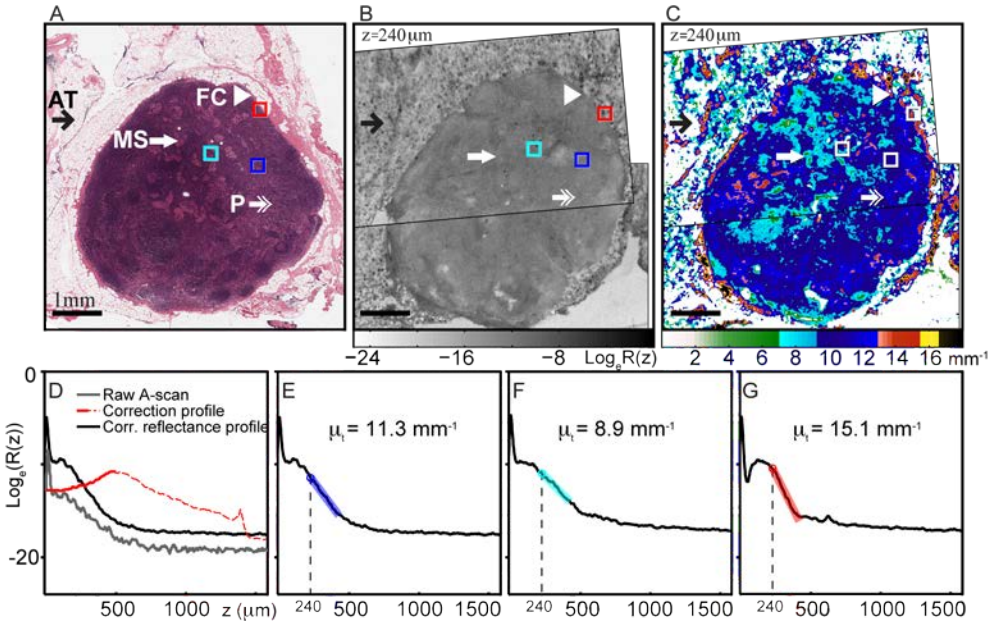


Fig. 2. Measured attenuation coefficients for a section of healthy lymph node. (**A**) Co-registered H&E-stained histology identifying tissue regions: MS, medullary sinuses (thick white arrow); P, paracortex (white double-headed arrow); FC, fibrous capsule (white arrowhead); and AT, adipose tissue (black arrow). (**B**) *En face* (*x*-*y*) OCT image at a depth of 240 μm from the window/tissue interface. Colored boxes at this depth indicate regions over which attenuation coefficients were measured. (**C**) Parametric image of measured attenuation coefficients ($mm^{-1}$) with a custom color map. Points with $R^2 < 0.7$ for the fit are excluded and are shown in white. (**D**) An example of the correction profile (red) used to generate a corrected reflectance profile (black) from its raw A-scan (grey). The dashed region of the correction profile is not used in the correction as the reflectance profile is below the noise floor for this region. Resulting averaged reflectance profiles at the centre of the colored boxes given in A and B and their linear fittings with $R^2 > 0.98$ are shown in: (**E**) paracortex (dark blue); (**F**) medullary sinuses (light blue); and (**G**) fibrous capsule (red). Signal peaks at $z = 0$ are due to specular reflection from the window/tissue interface. Scale bars = 1 mm.

#158284 - $15.00 USD Received 18 Nov 2011; revised 9 Jan 2012; accepted 18 Jan 2012; published 27 Jan 2012

of dense connective tissue. Pale-staining adipose tissue (AT) and some connective tissue surround the node.

In Fig. 2(B), two adjacent OCT images are superimposed. The OCT images show the perinodal adipose tissue is hyposcattering with a characteristic honeycomb appearance (light gray). Highly scattering curved regions at the periphery of the node are fibrous stroma of the capsule (dark gray). The lymphoid tissue exhibits medium scattering (gray) and is uniform in appearance. Features of interest within the lymphoid tissue, identified in the corresponding histology, are not obvious in the OCT image. There is evidence of external connective tissue in the perinodal adipose tissue, observable as linear reticulations of high scattering.

Mean attenuation coefficients, averaged within 30 $\mu m^2$ areas, were recorded for the selected regions of each tissue type that are indicated by the colored boxes in the co-registered histology and OCT images in Figs. 2(A) and (B), respectively. The histology section was determined to be approximately 240 μm beyond the tissue surface based on the depth of the corresponding *en face* OCT image. Examples of the averaged reflectance profiles, and resulting attenuation coefficient measurements, for the three lymphoid tissue regions described are presented in Figs. 2(e)-(g). The specular reflection from the glass window/tissue interface corresponds to $z = 0$. There is a slight gap between the glass window and the surface of the tissue that is occupied by PBS, which was used to reduce the refractive index mismatch as the light beam entered the tissue and to keep the tissue hydrated. For a region of paracortex (dark blue box and Fig. 2(e)) the attenuation coefficient was measured to have a mean of 11.3 $mm^{-1}$ and standard deviation of ±0.2 $mm^{-1}$ over the indicated area; for a medullary sinus (light blue box and Fig. 2(f)) $\mu_t = 8.7 \pm 0.4\ mm^{-1}$; and for a region of fibrous capsule (red box and Fig. 2(g)) $\mu_t = 14.8 \pm 0.5\ mm^{-1}$.

Attenuation coefficients were measured for each tissue type at three representative sample locations as identified in corresponding histology. Sample locations were chosen from all nine sections imaged in this study. However, not all sections contained each tissue type. The minimum and maximum attenuation coefficients obtained for each tissue type are presented in Fig. 3. Based on these ranges, thresholding was performed to generate a custom color map for segmenting tissue type and the resulting *en face* parametric image of attenuation is shown in Fig. 2(C). We observe segmented areas of medium attenuation (dark blue) in the outer area and a mixed low to medium attenuation (light blue) in the center upper area. This reflects the variation from paracortex to medulla seen in the histology. High attenuation (red), around sections of the node periphery, is attributed to the fibrous capsule. The outer region of perinodal adipose tissue has highly variable attenuation resulting from high standard errors of

| Tissue Type | Measured range* of $\mu_t$ ($mm^{-1}$) |
|---|---|
| Paracortex | 10.0 – 11.5 |
| Primary inactive cortical follicles | 4.5 – 6.8 |
| Medullary sinus | 8.1 – 9.1 |
| Fibrous capsule | 14.1 – 15.3 |
| Thickened fibrous capsule | 11.6 – 12.6 |
| Necrotic tissue | 13.0 – 14.5 |
| Dystrophic calcification | 16.0 – 16.5 |

*Measured at 1320 nm.

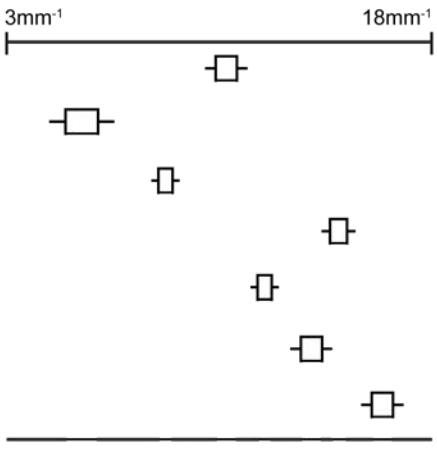


Fig. 3. Attenuation coefficient ranges for normal and reactive tissue regions in excised human axillary lymph nodes.

#158284 - $15.00 USD Received 18 Nov 2011; revised 9 Jan 2012; accepted 18 Jan 2012; published 27 Jan 2012

the regression (SER) for the least-squares fitting with $R^2 < 0.7$, so this region appears mostly white in the parametric images.

*4.2 Parametric imaging of lymph nodes*

Figures 4 and 5 present the results of parametric imaging demonstrating enhanced contrast of tissue types, as compared to *en face* OCT imaging. Figure 4 shows a lymph node with a prominent cortex and a fatty hilum. Of note in the histology image in Fig. 4(A) are mono-cellular regions of densely packed lymphocytes at the outermost region and a small central region of the node. These regions were identified as primary inactive cortical follicles (PF). The histology also shows clusters of unstained circular adipocytes (A) and gaps of lymphovascular spaces (LVS) cut in cross section and distinguishable from adipocytes by a thin wall of dense fibrous stroma. A thin fibrous capsule (FC) also lines the periphery of the node. A lighter-staining mottled region of paracortex (P) is evident as well as some medullary sinuses (MS) in the central region of the node. These regions are highlighted in the zoomed lower panels in Fig. 4. Several small vessels (V) can also be seen cut longitudinally in the paracortex in the magnified image.

The corresponding OCT image in Fig. 4(B) depicts scattering lymphoid tissue surrounded by hyposcattering adipose tissue with a diffuse border. High scattering is seen in some regions corresponding to the fibrous capsule, but artifacts caused by adipose tissue in superficial layers confound the border of adipose and lymphoid tissue. Artifacts (AF) account for much of the variation observed in the OCT image: high-signal (black) streaking from adipocytes can be seen in the upper left and center of the image, and artifacts due to shadowing from superficial vessels are evident in the paracortex. Within the node, some adipocytes and lymphovascular spaces are evident as white gaps corresponding with histology. Variable scattering within the node may be attributable to distinct tissue types, but the highlighted regions (boxes) do not show sufficient contrast to be distinguishable. Figure 4(C) presents a

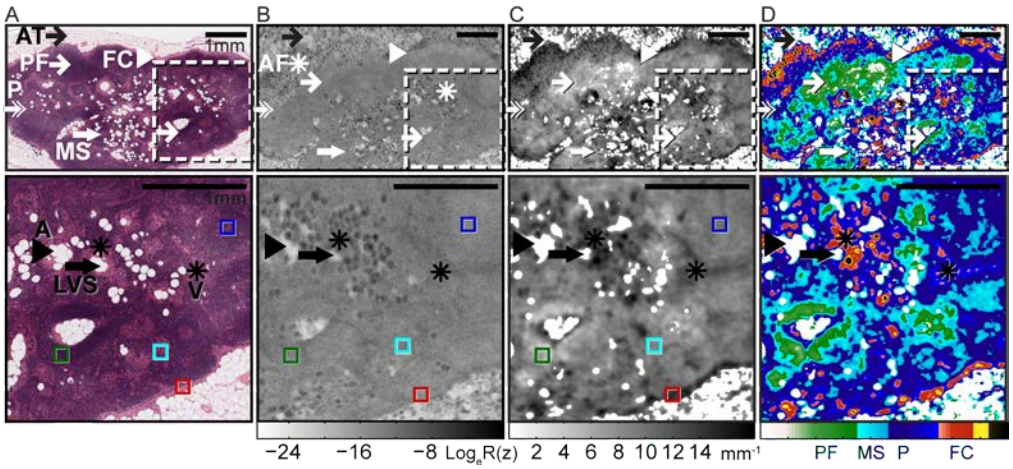


Fig. 4. Healthy lymph node with prominent cortex and fatty hilum. (**A**) Co-registered H&E-stained histology identifying tissue regions and features of interest: PF, primary inactive cortical follicles (thin white arrow); P, paracortex (white double-headed arrow); MS, medullary sinuses (thick white arrow); AT, adipose tissue (thin black arrow); FC, fibrous capsule (white arrowhead); A, adipocytes (black arrowhead); LVS, lymphovascular spaces (thick black arrow); V, vessels (black asterisk). (**B**) *En face* (*x*-*y*) OCT image at a depth of 240 μm from the window/tissue interface. Superficial adipocytes cause AF, artifact (white asterisk) in the OCT image. (**C**) Gray-scale parametric image of measured attenuation coefficients ($mm^{-1}$). (**D**) Parametric image presented with a custom color map. **Lower panels** 2.5 × magnified regions represented by white dashed boxes in the corresponding upper panels. Colored boxes indicate regions of distinct tissue type over which attenuation coefficients were measured: primary inactive cortical follicles (green); paracortex (dark blue); medullary sinus (light blue); fibrous capsule (red). Scale bars = 1 mm.

#158284 - $15.00 USD Received 18 Nov 2011; revised 9 Jan 2012; accepted 18 Jan 2012; published 27 Jan 2012

gray-scale parametric image of attenuation coefficients measured from the 3D-OCT data set. Compared with the OCT image (Fig. 4(B)), the parametric image displays greater contrast between the tissue regions of interest and improved identification of features such as vessels, adipocytes and lymphovascular spaces that correspond well with histology (Fig. 4(A)).

The vessel walls (V) are highly attenuating and are readily identified in the parametric images. Also of particular interest are regions of primary inactive cortical follicles, recognizable from their low attenuation (light gray) in the selected region (green box) with $\mu_t$ = 6.3 ± 0.5 mm$^{-1}$. The region of fibrous capsule (red box) has high attenuation (dark gray) $\mu_t$ = 14.4 ± 0.3 mm$^{-1}$. There is less contrast between the region of paracortex (dark blue box) $\mu_t$ = 10.6 ± 0.4 mm$^{-1}$ and medulla (light blue box) $\mu_t$ = 8.9 ± 0.2 mm$^{-1}$. Based on the measured attenuation coefficients these tissues can be quantitatively differentiated and segmented as depicted in Fig. 4(D). The custom color map, which is the same as used for Fig. 2, enhances the contrast between the paracortex and medullary regions and aids their differentiation. Comparing the parametric image of this node to that of the previous node in Fig. 2, we see that the classification of tissue type is consistent.

Figure 5 presents results from a lymph node that is reactive in response to adjuvant therapy for pre-operative tumor treatment. The histology image in Fig. 5(A) shows a localized region of necrotic tissue (N) with dystrophic calcifications (C), highlighted by the beige and yellow boxes respectively. The necrotic tissue is interpreted to be treated tumor cells and has a uniform, pink-staining, fragmented appearance. The core of the necrotic area contains dark-purple staining foci of calcifications. There is a loss of normal tissue architecture in response

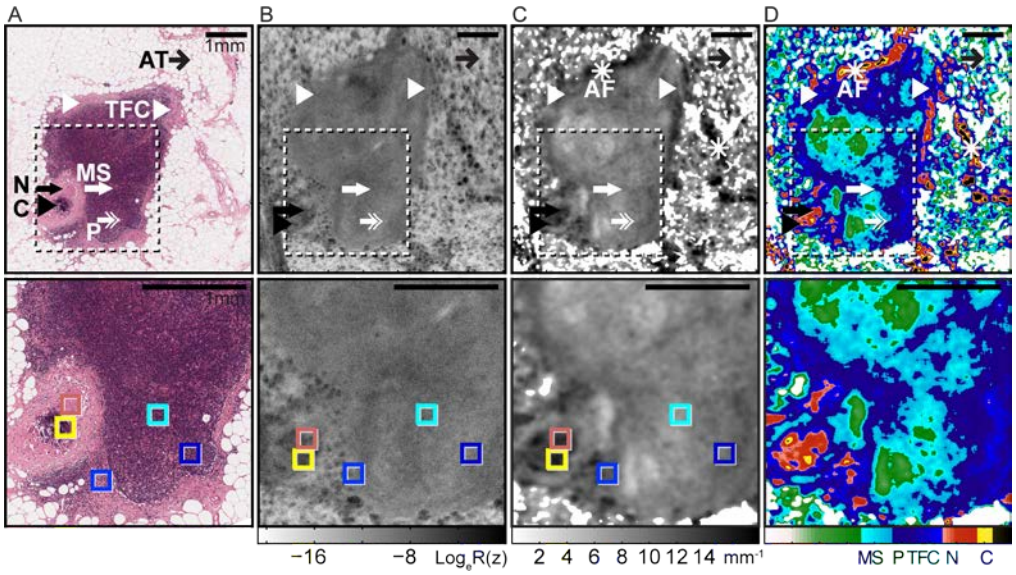


Fig. 5. Reactive lymph node with an area of necrotic tissue containing dystrophic calcifications and a loss of normal tissue architecture. (**A**) Co-registered H&E-stained histology identifying tissue regions of interest: N, necrotic tissue (thick black arrow), C, calcifications (black arrowhead), TFC, thickened fibrous capsule (white arrowhead); AT, adipose tissue (thin black arrow), P, paracortex (white double-headed arrow), MS, medullary sinuses (thick white arrow). (**B**) *En face* (*x*-*y*) OCT image at a depth of 240 μm from the window/tissue interface. (**C**) Gray-scale parametric image of measured attenuation coefficients (mm$^{-1}$). Sharp tissue interfaces particularly at the capsule cause AF, artifacts (white asterisk) in the attenuation measurement. (**D**) Parametric image of attenuation coefficients presented with a custom color map. **Lower panels** 2 × magnified regions represented by white dashed boxes in the corresponding upper panels and colored boxes indicate regions of distinct tissue type over which attenuation coefficients were measured: necrotic tissue (beige); foci of dystrophic calcification (yellow); thickened fibrous capsule (blue); medullary sinus (light blue); paracortex (dark blue). Scale bars = 1mm.

#158284 - $15.00 USD Received 18 Nov 2011; revised 9 Jan 2012; accepted 18 Jan 2012; published 27 Jan 2012

to the necrotic tissue, including a fibrous border around the necrotic site, a thickened fibrous capsule (TFC) and a medulla with constricted sinuses (MS) making it difficult to distinguish.

The OCT image in Fig. 5(B) exhibits imaging artifacts caused by streaking of superficial adipocytes that make it difficult to delineate the capsule. There is high scattering in the external adipose tissue, which is in agreement with the presence of connective tissue in the corresponding areas in the histology. The necrotic tissue is not well distinguished due to these artifacts and it is unclear if it is part of the lymphoid region or part of the external connective tissue.

The grayscale parametric image in Fig. 5(C) clearly depicts the necrotic region and calcifications by the high contrast in their attenuation coefficients. A region of necrotic tissue (orange box) has high attenuation (dark gray) $\mu_t$ = 13.4 ± 0.4 mm$^{-1}$ and a focus of calcification (yellow box) has very high attenuation (black) $\mu_t$ = 16.0 ± 0.4 mm$^{-1}$. Thus, distinction of the necrotic tissue is possible using parametric imaging. Unique identification may be compromised when compared to areas of the capsule showing similar attenuation, such as the upper border. However, this region also exhibits artifacts that are not present in the necrotic tissue, observable as outliers of hyper-attenuation displayed as black in the color-mapped parametric image in Fig. 5(D). Such outliers are due to the sharp interface from one tissue type to another, especially the interface to the thin fibrous stroma of the capsule, where the fitting range is larger than the distance over which the tissue extends. Improvement of the method is needed to increase the specificity for differentiating necrotic and capsular tissue.

The parametric image in Fig. 5(D) presents the thickened reactive fibrous capsule (blue) with lower attenuation, $\mu_t$ = 11.8 ± 0.2 mm$^{-1}$, than normal anatomical capsule (red). It is present around the left and lower periphery of the node, while areas of intact normal capsule remain at the upper and right borders of the node, in agreement with histology. The paracortex (dark blue) has similar attenuation to the thickened capsule with $\mu_t$ = 10.4 ± 0.4 mm$^{-1}$, which is consistent with a greater population of lymphocytes and less collagen in these areas. The fibrous border around the necrotic tissue exhibits attenuation overlapping both paracortical and medullary ranges (light blue to dark blue). It is evidently a different tissue type though not uniquely distinguished by its attenuation. Finally, we observe low attenuation in the center-most region, which is consistent with medulla $\mu_t$ = 8.3 ± 0.2 mm$^{-1}$, although there is very low attenuation in the center of the medulla that suggests a separate composition. There may be two reasons for this: firstly, the section was cut at an angle to the *en face* OCT image plane so that the variation may not match to the plane of histology shown; secondly, the tissue in this region may be subtly different in its architecture and morphology than either paracortical or medullary tissue, but not so well defined in the histology that it can be classified. Improved correlation to histology is needed in this case to determine the tissue type and how it differs in morphology from other regions. The current study concentrates on establishing the basic feasibility of the method but a more extensive study will be required to resolve such ambiguities.

## 5. Discussion

### *5.1 Attenuation coefficients and parametric imaging*

We have used OCT to measure absolute, localized attenuation coefficients of healthy inactive and reactive human axillary lymph nodes. Based on these measurements, we have generated parametric images of the attenuation coefficient and correlated these with histology to identify the characteristic attenuation coefficients for selected tissue types. Attenuation coefficients within normal lymph nodes ranged from 4.5 to 15.3 mm$^{-1}$. The lowest measured attenuation coefficient was $\mu_t$ = 4.5 mm$^{-1}$ for regions of primary inactive cortical follicles. Regions of paracortex and medullary sinuses had intermediate attenuation coefficients ranging from 8.1 to 11.5 mm$^{-1}$. High attenuation $\mu_t$ > 14 mm$^{-1}$ was measured for the fibrous capsule in all of the samples. In comparison, reactive thickened fibrous capsule in a node containing an area of

#158284 - $15.00 USD Received 18 Nov 2011; revised 9 Jan 2012; accepted 18 Jan 2012; published 27 Jan 2012

necrotic tissue had a slightly lower attenuation coefficient $\mu_t \approx 12 \text{mm}^{-1}$. Importantly, these measured attenuation coefficients are system-independent and absolute since, having accounted for the system confocal and OCT depth scan responses, the signal decay is a direct measure of tissue attenuation.

In the node containing necrotic tissue, which was interpreted to represent a reaction to pre-operative therapy, high attenuation was measured for the necrotic region $\mu_t \approx 13$ mm$^{-1}$ and very high attenuation was measured for foci of dystrophic calcifications $\mu_t > 16$ mm$^{-1}$. The necrotic tissue in this case was the result of adjuvant therapy, but regions of necrotic tissue are also observed in metastatic deposits of untreated breast cancer. We expect the attenuation characteristics for malignant metastatic deposits to be higher than normal lymphoid tissue, as indicated in the results from this study and from the results in [23]. This is expected since metastatic deposits have enlarged cells with increased organelle and cell density, contributing to increased scattering.

Our results show good agreement with previously reported measurements of attenuation coefficients in soft tissues: human arteries with atherosclerotic plaques, measured with OCT at 800 nm, gave $\mu_t$ = 3.2 to 9.5 mm$^{-1}$ for normal arterial tissue; $\mu_t$ = 11.1 mm$^{-1}$ for calcified plaques [18]; and at 1310 nm $\mu_t$ >10 mm$^{-1}$ for necrotic core [30]. Similarly for normal porcine arterial tissue at 1320nm, $\mu_t$ ranged from 1.19 to 15.88 mm$^{-1}$ [36]. Measurements of light transmission in breast tissue gave an attenuation coefficient of $\mu_t$ = 8.3 ± 2.0 mm$^{-1}$ at 830 nm [37]. Also the median attenuation coefficient measured using OCT at 1300 nm for normal renal tissue was $\mu_t$ = 4.95 mm$^{-1}$ and for renal cell carcinoma was $\mu_t$ = 8.86 mm$^{-1}$ [22]. While necrotic tissue was found to have high optical attenuation, it was observed to be lower than healthy fibrous tissue (i.e. fibrous capsule, Fig. 3). This is in agreement with earlier work which induced necrosis in human fibroblasts, and found necrotic cells exhibited a corresponding decrease in attenuation [38].

The attenuation coefficient of the tissue types presented here aids differentiation, however, it is not always a unique identifier. We also take into account the locations and geometries in correctly identifying tissue types. The fibrous capsule, for example, is distinguishable from necrotic tissue by its thin curved appearance, and follicular tissue, which lies in the cortical area, is distinct from medullary sinuses, which lie away from the periphery. More accurate differentiation of tissue types is possible by interpreting localized attenuation coefficients in combination with morphological appearance in the parametric images. The color mapping of parametric images, as presented here, enhances contrast and improves the ability to visually identify tissue type. Similar conclusions have been drawn in parametric imaging of atherosclerotic plaques [18,25,30]. In comparison, methods based on point-by-point optical parameter measurement must rely on obvious differences in optical properties, such as between adipose and fibrous tissue [39,40], or else use computational analysis to efficiently assess many parameters simultaneously [17,41,42]. We note that an extension to two-parameter imaging was recently demonstrated in atherosclerotic plaques and in tissues of the anterior eye [26] and showed further improvement in tissue contrast and characterization beyond that achieved with one-parameter mapping.

### *5.2 Methods, study limitations and future work*

The single scattering model, modulated for confocal and scanning corrections, proved robust and adequate for measuring and differentiating the attenuation coefficients of human lymph node tissues at low optical depth. The analysis and parametric imaging algorithms may be improved by further optimization, such as increasing the number of averaged A-scans for greater speckle reduction, or altering the fitting range based on the expected homogeneity of selected regions. Though our fitting range was kept constant at 200 μm, we moved this range over all locations, finding the maximum number of homogeneous regions for which it was

#158284 - $15.00 USD Received 18 Nov 2011; revised 9 Jan 2012; accepted 18 Jan 2012; published 27 Jan 2012

applicable in three dimensions, and excluding those for which it was not ($R^2 < 0.7$ in images, $R^2 < 0.98$ in tabulated values).

A limitation of the method reported here was the speed of acquisition and processing. The presented images were obtained from *ex vivo* samples using a TD-OCT system with high image quality, but slow acquisition speed. The method is readily transferable to higher scan speed spectral-domain OCT systems to address this issue. Processing of large 3D data sets (3.5 × 6 × 2 mm) is also computationally intensive but lends itself to optimization through highly parallel algorithm implementation. The issue of *in vivo* imaging has been addressed separately [43] by using miniature probes incorporated into needles to increase penetration depth, implemented using a portable spectral-domain OCT system.

Co-registration of the histology was made difficult in some cases because of tissue deformation and shrinkage caused by the fixation, processing and mounting procedures [44] [45]. We sampled the histology sections at a depth of approximately 200 μm, but distortion during histological processing meant that the histology section did not necessarily correspond to a flat plane in the OCT scan of the fresh tissue. Co-registration with histology was generally easier with the parametric images than with OCT, since the contrast between tissues was improved. Artifacts in the parametric images were still present but were less disruptive than those affecting OCT because of the improved contrast between different tissue types. Artifacts were observed when the computed parameters corresponded to heterogeneous regions of tissue. This also occurred where tissue structures were very thin, such as the lymph node capsule. We attempted to exclude regions of inhomogeneity from the images by rejecting fits with high standard errors of the regression. An alternative technique has also been proposed in which fitting was performed over a variable range until a decrease in fit quality was observed [30].

The results presented here represent a baseline in the use of this technique and are a first step towards establishing its use in a clinical setting. The promise of the results suggests that a larger study with more patients and more sampling regions is warranted. Such an expanded study would help to establish statistical accuracy as well as improve the accuracy and reliability of the thresholding map.

## 6. Conclusions

In this paper, we have reported a method to characterize and improve differentiation of healthy and reactive tissue types in human axillary lymph nodes using parametric imaging. The method uses a single-scattering model of OCT to measure attenuation coefficients at low depths. We applied this model to *ex vivo* lymph node sections to measure the attenuation coefficients of medullary sinuses, paracortex, primary inactive cortical follicles, fibrous capsule, necrotic tissue and dystrophic calcifications. We showed that parametric imaging of the attenuation coefficient enables enhanced differentiation of these tissue types compared to standard OCT. Based on previous OCT imaging of lymph nodes, we expect that cancer metastasis will be detectable based on high attenuation and we have measured attenuation in healthy and reactive nodes as a first step towards this. Since the presented analysis is based on quantification of intrinsic tissue attenuation, contrast is transferable between samples and between scans with minimal effect from system variations. We believe this methodology provides an important improvement to OCT imaging of lymph node morphology and is a step towards *in situ* assessment of lymph nodes using OCT.

## Acknowledgments

Loretta Scolaro acknowledges the support of the William & Marlene Schrader Postgraduate Scholarship to undertake this work. Robert A. McLaughlin is supported by a fellowship from the Cancer Council Western Australia and funding from the National Breast Cancer Foundation, Australia